AFM-Raman

Correlated TERS, TEPL and SPM Measurements of 2D Materials

Agnès Tempez[1], Ophélie Lancry[1], Andrey Krayev[2] & Marc Chaigneau[1]
[1]HORIBA France SAS, Palaiseau, France, [2]HORIBA Instruments, Inc. Irvine, CA, USA

Abstract : This application note reports on **nano-characterization** of 2D transition metal dichalcogenides (TMDCs) materials which are considered of very high potential semiconductors for future nanosized electronic and optoelectronic devices. Scanning probe microscopy (SPM) giving access to the critical topographic and electronic properties at the nanoscale is coupled to photoluminescence (PL) and Raman spectroscopies by means of plasmon enhancement to yield **correlated electrical and chemical information down to the nanoscale.**

Keywords : AFM-Raman – 2D materials – Transition metal dichalcogenides (TMDCs) – TERS – TEPL – Heterogeneities – Nanomaterials – Opto-electronics – Heterojunctions

Context and issues

2D materials are defined as crystalline materials consisting of a single unit cell layer of that material. Among the large number of potentially stable 2D materials (more than 700), graphene and the family of transition metal dichalcogenides (TMDCs) are under thorough study as candidates for tomorrow's nanoelectronics building blocks. Monolayer TMDCs are tunable band gap semiconductors and complement zero gap graphene. A myriad of nanoelectronics applications are foreseen, ranging from transistors to photodetectors as well as in the energy field (nanogenerators, green electronics, electrocatalytic hydrogen generation and energy storage).

Many challenges remain before the promise of 2D materials is realized in the form of practical nano-devices, e.g.: (i) understanding growth mechanism of these crystals, to be able to fabricate defect-free large area film, (ii) controlling transfer processes from growth substrates to other substrates, (iii) controlling their vertical or lateral integration. An information-rich, **nanoscale characterization technique** is required to qualify these materials and assist in the deployment of 2D material-based applications.

Raman and photoluminescence spectroscopies are the techniques of choice to characterize monolayer crystalline materials in terms of electronic behavior (band gap, carrier concentration) and structural quality (defect location and density). Because these conventional spectroscopies are far-field optical techniques (the spot size is diffraction-limited), their applications are restricted to the micro- and macro-worlds. Plasmon-enhanced optical spectroscopies (TEPL: Tip-Enhanced Photoluminescence, TERS: Tip-Enhanced Raman Spectroscopy) bridge the gap to NanoPL and NanoRaman and offer optical nanometric spatial resolution.

These new spectroscopic techniques can now be combined with other SPM modes for multi-parameter analysis of 2D materials [1,2]. The work presented in this article opens up new possibilities for the characterization of chemical, optoelectronic, topographic and electronic properties of 2D materials.

Correlated TEPL and SPM of MoS$_2$ flakes on Au/Si substrate

Molybdenum disulfide (MoS$_2$) is a promising semiconducting transition metal dichalcogenide 2D material for next generation photovoltaic solar cells, optoelectronic circuits and sensors due to its great excitonic recombination property, high carrier mobility and low leakage current. One of the advantages of two dimensional TMDCs, e.g. with respect to graphene, comes from quantum confinement, enabling the indirect-to-direct band-gap transition as a function of number of individual layers. Nano-scale characterization is needed to provide the understanding necessary to engineer nanodevices integrating monolayer MoS$_2$.

Monolayer MoS$_2$ has a band gap about 1.8 eV, as revealed by photoluminescence (PL) spectroscopic analysis. The PL spectrum is decomposed in two peaks due to excitonic features: the A$_0$ mode derived from an exciton consisting of one electron and one hole bound by Coulomb interaction and the A$^-$ mode derived from a trion, a charged three-body exciton consisting of an exciton combined with another electron. It has been reported that the PL intensity decreases with increasing number of MoS$_2$ layers and that the PL intensity to Raman intensity ratio is related to the number of layers [3].

Tip-enhanced optical spectroscopies based on the amplification of signal from the nano-region under the SPM tip will allow for actual nano-characterization. In the case of TMDCs, Tip-Enhanced Photoluminescence (TEPL) is capable of revealing variation in emission within a submicron size flake. Complementary morphological, chemical, and electronic structure information may be acquired simultaneously – and with nanometer spatial resolution – through AFM imaging.

TEPL measurements are performed on MoS_2 flakes transferred to a gold-on-silicon substrate using a NanoRaman™ system from HORIBA Scientific integrating an Atomic Force Microscope (AFM) (OmegaScope, based on SmartSPM) and a Raman microscope (XploRA) with a ×100 WD objective tilted by 60° with respect to the sample plane. A 638 nm p-polarized laser is focused onto the cantilever-based silver coated TERS tip (OMNI TERS-FM probe). An AFM topography map is first recorded to locate MoS_2 flakes, as well as to provide electrical analysis with KPFM (Kelvin Probe Force Microscopy) giving the contact potential difference (CPD) and capacitance using a silver coated tip in frequency modulation mode (15 nm lift in dual pass setup) (Fig. 1).
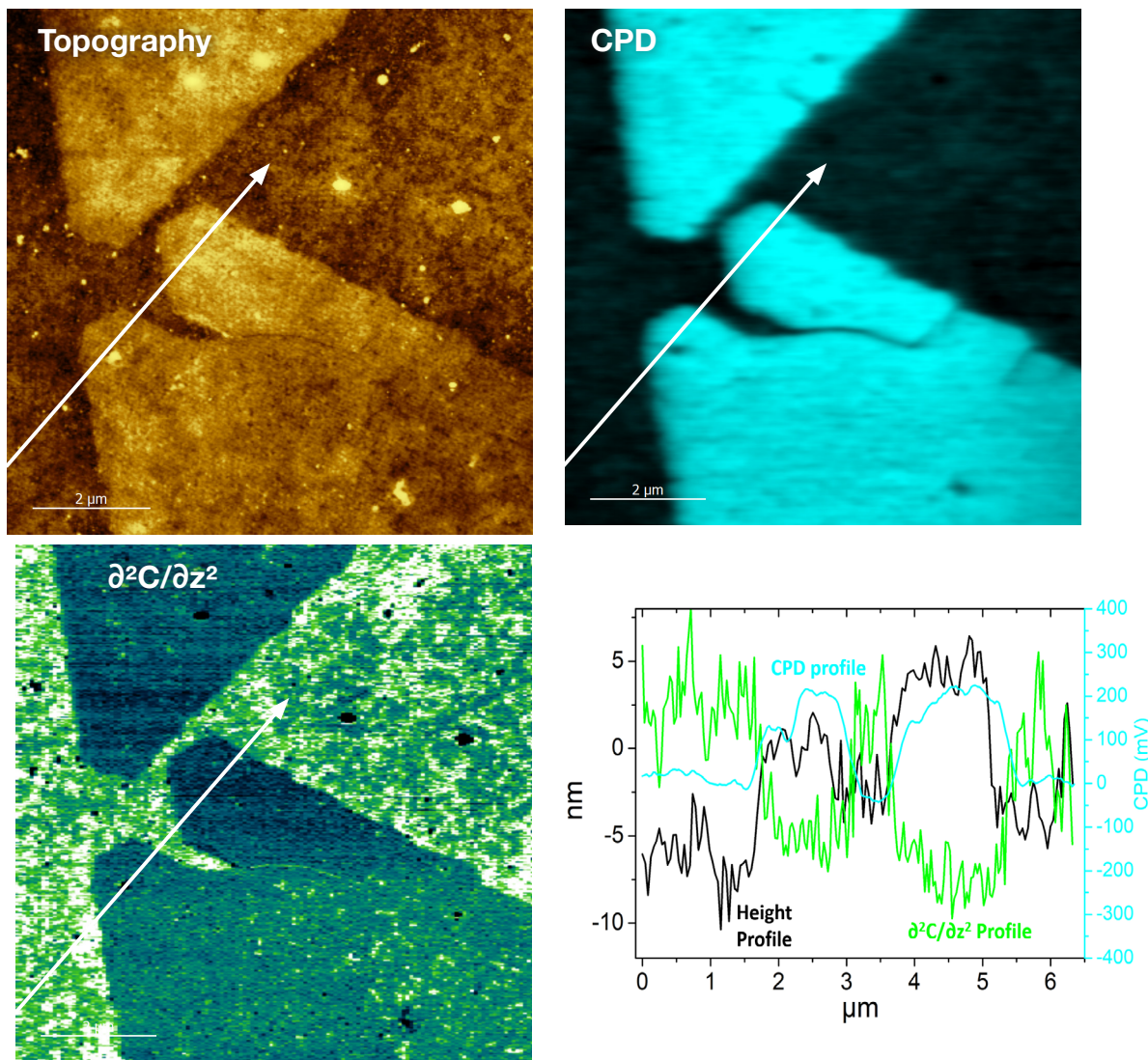

Figure 1: AFM topography, CPD and capacitance measurements on MoS_2 flakes on Au/Si substrate. The lower right graph shows section analysis (topography, CPD and capacitance) along the white arrows displayed on the different AFM images.

Here, as with other 2D materials, it is key to correlate electronic characteristics with nanoscale excitonic and chemical properties provided respectively by TEPL and TERS measurements [3-6]. A PL map of the same two flake apexes (6 × 9 µm (60 × 90 pixels)) is collected with a 100 ms integration time spectrum (640-840 nm) at each pixel (100 nm step). Two PL maps are actually recorded together with topography in a special mode called "Spec-Top™" mode with "dual spec" option: for each pixel (i) one spectrum (sum of the near-field and far-field signals) is acquired with tip in direct contact with the surface with a typical interaction force of 2-10 nN and (ii) another spectrum is acquired with tip in tapping mode (a few nm away from the sample surface, considered to be the far-field contribution). In between two pixels of the map, the sample moves in semi-contact mode to preserve the sharpness and plasmonic enhancement of the tip.
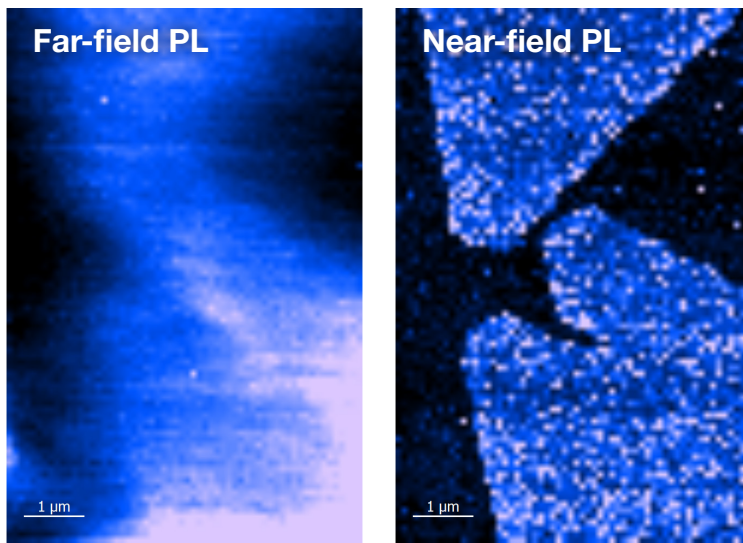
Figure 2: (left) Conventional far-field Photoluminescence map and (right) NanoPL (or TEPL) map of the same MoS₂ flakes.

Two PL maps are shown in Fig. 2, the as-acquired far-field PL map ("tip up") and the near-field or true NanoPL map (TEPL) generated upon subtracting the far-field spectrum ("tip up") from the spectrum in contact (far-field + near-field or "tip down") for each pixel. Both PL images are generated from the integration of PL band from 640 to 740 nm. The improved spatial resolution in the TEPL image (right) compared with the far-field PL image can be clearly seen: the edges of the flake, indistinguishable in the conventional far-field microPL image are perfectly defined in the TEPL image. In addition, as shown in the overlay with the topography (Fig. 3), edges perfectly match those of the AFM height image. Two spectra are plotted in the graph of Fig. 3 from averaging 4-pixels, one from interior of the flake **(red)** and from the substrate **(blue)**. A Gaussian fit gives a peak at 660 nm (1.88

eV) which corresponds to the band gap of monolayer MoS₂. The topography profile indicates an apparent thickness that is much higher (~4-6 nm) than the expected monolayer thickness (0.8 nm), which is likely due to the roughness of the gold surface (RMS = 3 nm) onto which the flake was transferred.

This first example of TEPL on MoS₂ shows that TEPL method, not limited by diffraction, provides a drastic improvement of the optical resolution compared to far-field photoluminescence (microPL) and is also more accurate than AFM topographic imaging to confirm the presence of monolayer flakes. The next sections of this article will demonstrate how TEPL and TERS are capable of revealing nanoscale heterogeneities impossible to access with conventional optical techniques.
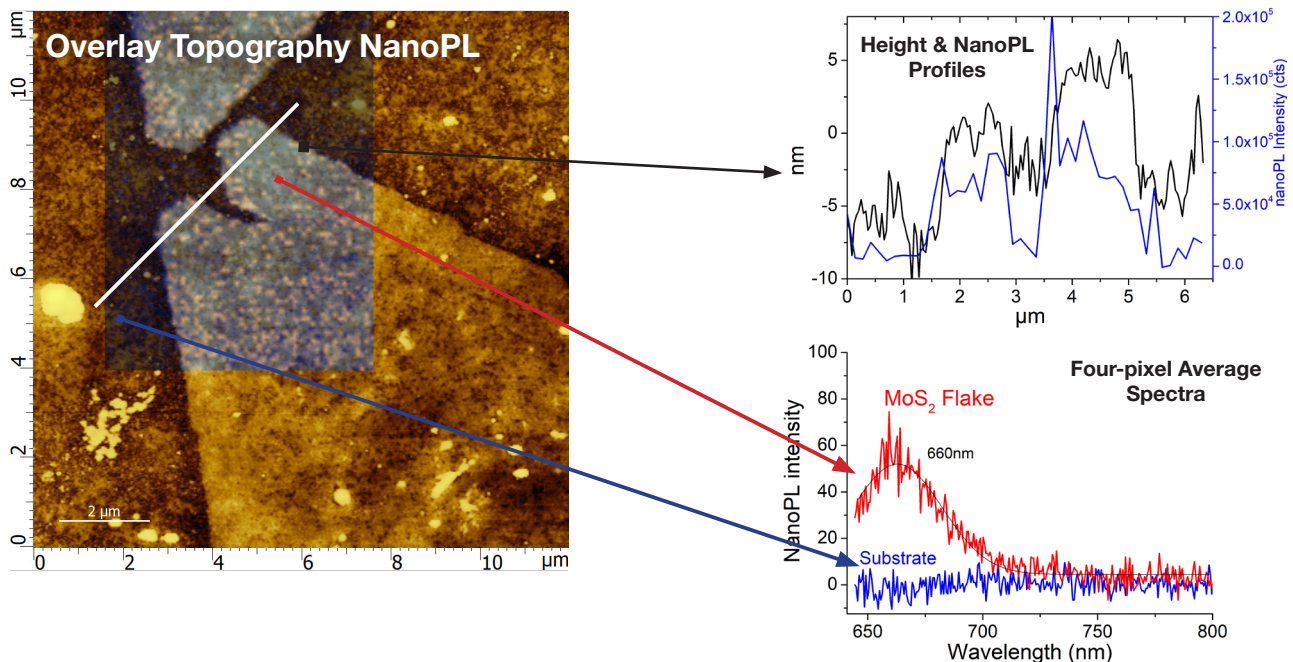

Figure 3: (left) Overlay of the AFM topography and TEPL images of MoS₂ flakes, (top right) AFM height and TEPL section analysis and (lower right) TEPL spectrum from interior of the flake and from the substrate.

TEPL measurements of WS$_2$ flakes on SiO$_2$/Si

Tungsten is the largest and heaviest transition metal in the family of common transition metals and in contrast with molybdenum, is more abundant in the Earth's crust, cheaper, and less toxic. Monolayer tungsten disulfide (WS$_2$) is a direct-gap semiconductor with an energy gap close to 2 eV and high photoluminescence quantum yield ($\approx$ 6%) (higher compared to other 2D semiconductors, e.g. $\approx$ 0.1% in monolayer MoS$_2$). It has also exceptional properties such as large spin–orbit coupling ($\approx$ 420 meV), large exciton/trion binding energy, and nonblinking photon emission. The most common stacking structure of WS$_2$ is 2H, in which the W atoms of a given layer are sitting exactly on top of the S atoms of its neighboring layer.

In this section, correlated AFM and TEPL measurements are performed on WS$_2$ flakes grown pseudo-epitaxially on a silica on silicon (SiO$_2$/Si) substrate using a NanoRaman™ system integrating an Atomic Force Microscope (OmegaScope) with a confocal Raman LabRAM HR Evolution microscope. A 532 nm *p*-polarized laser is focused onto the cantilever-based silver coated TERS tip.

Fig. 4. shows AFM topography of a 14 μm triangular flake with 512 lines resolution. Far-field (FF) and near-field + far-field (NF+FF) maps are acquired with 500 ms integration time spectra and steps of 93 nm. PL images are generated from the integration of PL tail from 640 nm to 690 nm. Fig. 4 shows two PL images: the as-acquired far-field and the near-field or TEPL calculated from subtraction of FF map from NF+FF map. One can observe the higher resolution of the TEPL image with respect to the far-field image.

(i)   The contour of the triangular single crystalline flake as well as that of the thicker inner center triangle are much more well defined in the TEPL map than in the far-field image.

(ii) Dark spots of size ranging from 100 nm to 200 nm can clearly be seen in the TEPL map. They are likely to be nanocrystallites visible as bright features of few tens of nm of height in the AFM topography image.

(iii) The PL response non-uniformity on the outer monolayer part of the flake is resolved at the nanoscale, which reveals a lot of inhomogeneities.
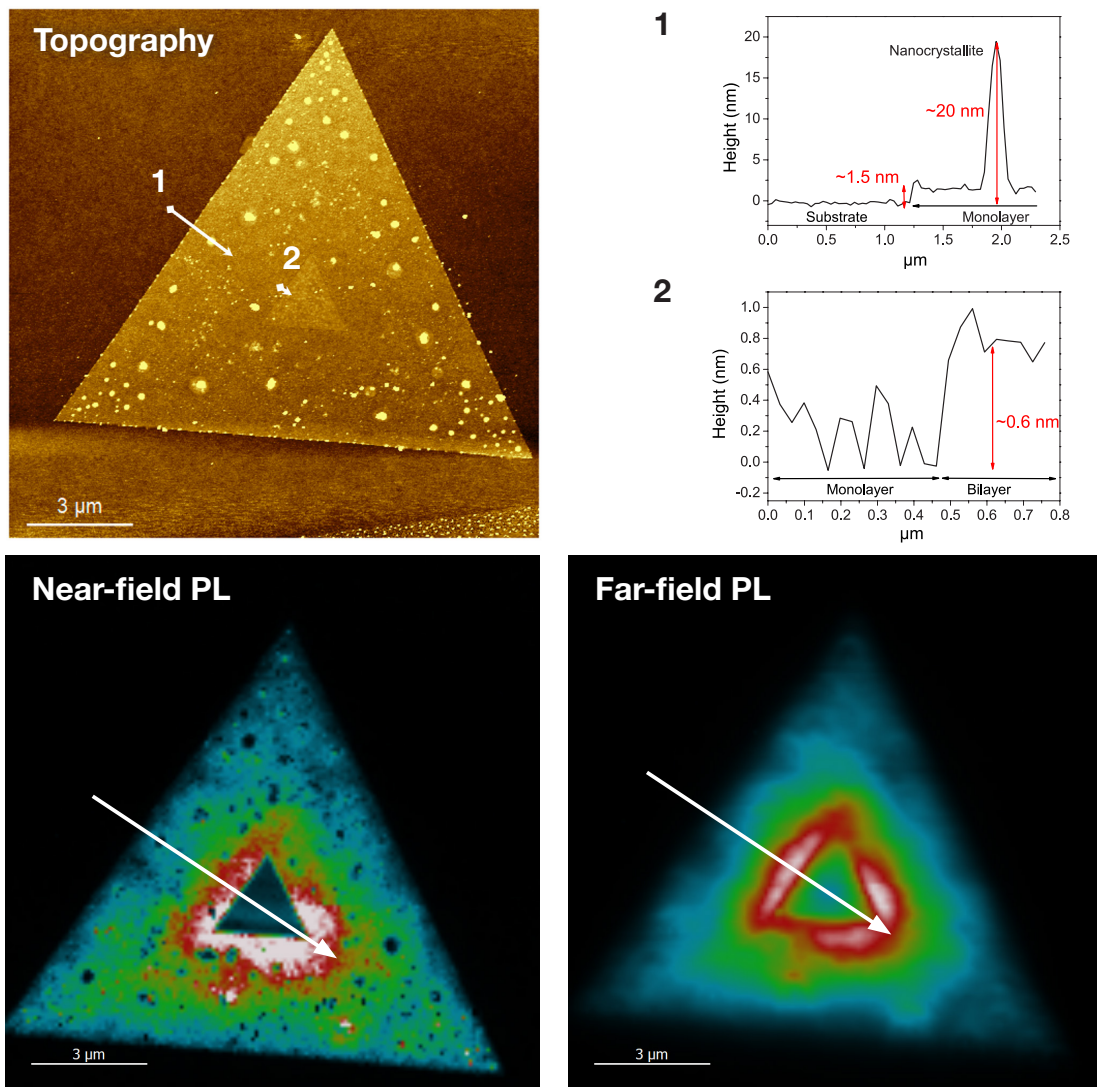

Figure 4: Topography, near-field and far-field PL images of WS$_2$ flake on SiO$_2$/Si. The upper right graphs show two section analysis done along the arrows 1 and 2 shown on the AFM topographic image.

This higher resolution is also demonstrated through the comparison of the PL intensity profiles crossing the flake through the inner center triangle showing (Fig. 5):

(i)   Abrupt rise going from substrate onto the monolayer WS$_2$ flake in the near-field profile compared to slow rise in the far-field.
(ii) More pronounced dip in the near-field profile when crossing the ~20 nm high nanocrystallite (height profile "1" in Fig. 4) than in the far-field profile.
(iii) More abrupt decrease (higher than one order of magnitude) going from monolayer to bilayer (height profile "2" in Fig. 4 shows a 0.6 nm difference) in the near-field than in the far-field profile.
(iv) A tremendous gain in signal to noise ratio: the dynamics goes from 1.5 decades in far-field to more than 5 orders of magnitude in near-field PL.

TEPL reveals deep sub-diffraction limit details within the 2D WS$_2$ flake that are not resolved in conventional PL measurements [7,8]. Edge effects, nanocrystallites, grain boundaries etc. are seen in the TEPL image with improved signal to noise ratio and vastly improved resolution.
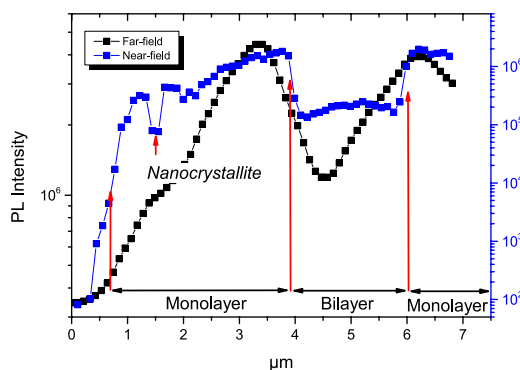

Figure 5: Section analysis of the PL signal in far-field (black) and in near-field (blue) along the arrows represented in Fig. 4.

Correlated TEPL and SPM of WSe$_2$ flakes on SiO$_2$/Si

As a 2D material, WSe$_2$ consists in a layer of tungsten atoms sandwiched between two layers of selenium atoms. When the thickness of a WSe$_2$ crystal is reduced from bulk to monolayer (1L), its energy band transitions from indirect (band gap ~ 1.2 eV) to direct (band gap ~ 1.7 eV). 1L WSe$_2$ possesses a high exciton binding energy (~790 meV), high PL quantum yield (QY, 10%) and long photoluminescence (PL) lifetime (up to nanoseconds), which are superior to 1L MoS$_2$ and WS$_2$. Furthermore, 1L WSe$_2$ exhibits natural p-type doping, ultra-low thermal conductivity (0.05 W m^{-1}K^{-1}) and high carrier mobility (>100 cm^2 V^{-1}S^{-1}). This combination of properties makes 1L WSe$_2$ a promising candidate for novel optoelectronic devices such as high QY light emitting diodes and quantum light sources. The development and implementation of WSe$_2$ 2D applications require an optical characterization technique on the order of tens of nanometers. Correlated TEPL and SPM provide substantial information related to the nanoscale optical properties of WSe$_2$ with a resolution down to a few nanometers [9].

These measurements were performed using the same NanoRaman™ system from HORIBA Scientific described in the previous sections of this article. An optical image (Fig 6a) of the entire sample (20×8 mm) is first obtained under the Raman microscope using the mosaic mode (10× objective images are rapidly acquired and stitched). With this full view of the entire sample and the top-view image of the OmegaScope top camera (10× objective), navigation on the sample positioned for correlative SPM measurements is facilitated. It becomes easy to identify and reach areas of interest (Fig. 6b).
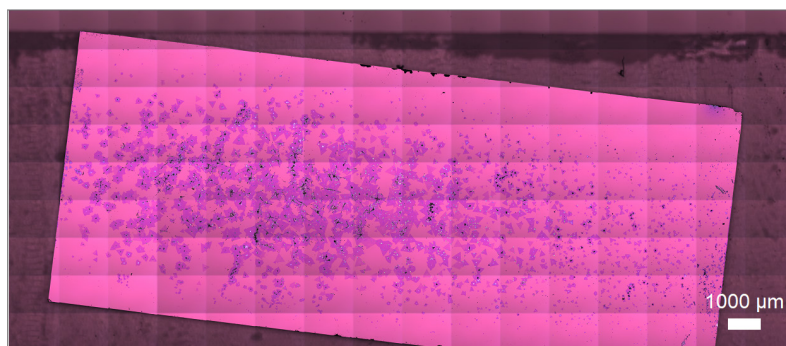

Figure 6a: Optical image of entire sample of WSe$_2$ on SiO$_2$/Si obtained with Raman microscope using Mosaic mode.
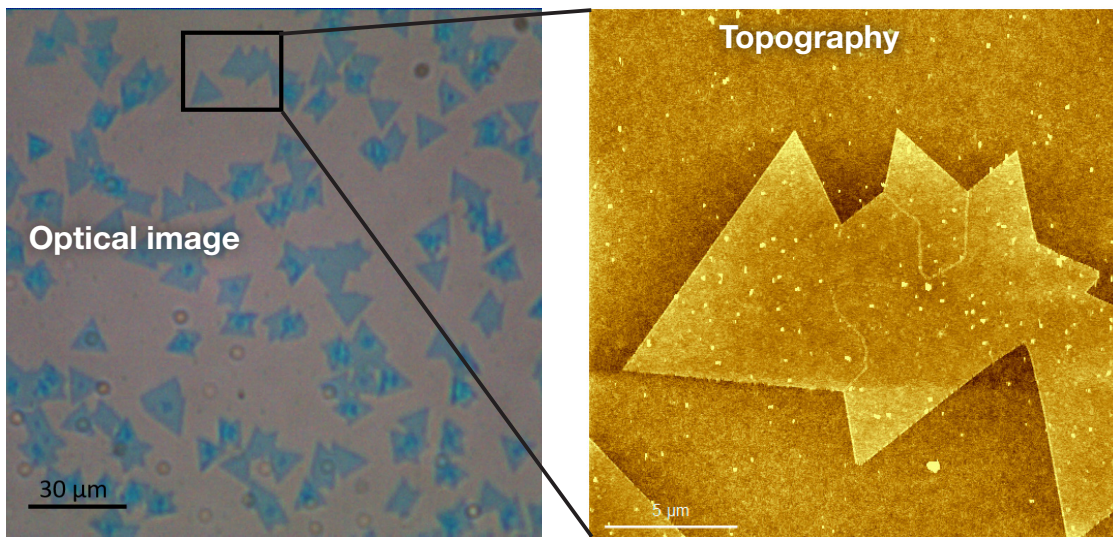
Figure 6b: Optical and AFM topographic images of WSe$_2$ flake on SiO$_2$/Si.

The OmegaScope top-view image shows a region of interest, which is then selected for detailed analysis: several monolayer triangular flakes (clearly observed in a light blue color) that have merged. The corresponding AFM topography image (20×20 µm, 512 lines) shows a fraction of a large polygon flake consisting of several merged triangular flakes with different orientations. The bright spots on the flake are overlying nanocrystallites. On this high-resolution topography AFM image, some grain boundaries (GB) are also discerned.

Two PL maps are acquired corresponding to "near-field + far-field" (NF+FF) and "far-field" (FF) using "*Spec-Top^{TM}*" mode with "dual spec" option. The acquisition time of each spectrum was 50 ms and pixel size 116 nm. The "dual spec" option gives access to the true TEPL map upon subtraction of FF map from the NF+FF map.

Fig. 6c shows the far-field and near-field PL images generated from integration of the PL band from 700 to 800 nm.

The far-field image with an optical resolution of 550 nm shows some variation of PL intensity over the large 20 µm size polygonal flake with lower PL along the edges and GB than in the center of the flakes. However, this far-field image cannot render nanoscale excitonic variations due to the optical diffraction limit; the higher resolution pure near-field TEPL image reveals much more details (Fig. 6c):

(i)   Much sharper edges.
(ii)   A distinct 800 nm wide lower PL (30% quenching) edge all around the flakes.
(iii)   Clearly defined grain boundaries but appearing with different contrast (PL is quenched with different ratio depending on tilting angle between two merging flakes).
(iv)   Dark spots (10% of center flake PL intensity) of size less than 200 nm corresponding to overlying nanocrystallites also observed in the topography image.
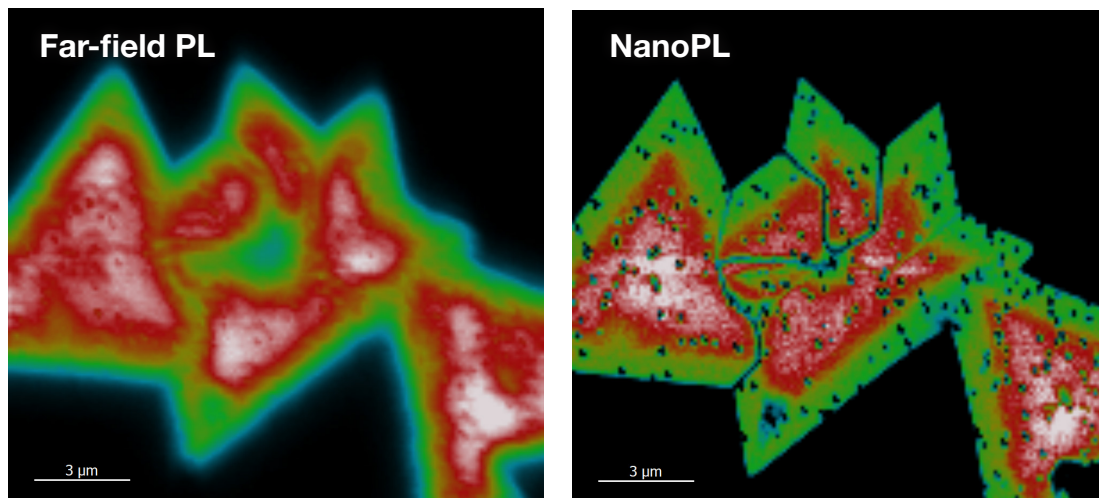

Figure 6c: Conventional far-field PL and TEPL images of WSe$_2$ flake on SiO$_2$/Si.

Average spectra taken from center and edge areas show TEPL quenching and slight red shift of edge with respect to center (Δ = 17 meV) (see graph in Fig. 7). TEPL spectra taken from several nanocrystallites and along a GB exhibit much lower intensity and broader peaks. This TEPL measurement, showing different spectral signatures, reveals a nanoscale excitonic heterogeneity. These optoelectronic properties of WSe_2 can be further studied using the combination of TEPL and Kelvin Probe Force Microscopy (KPFM).
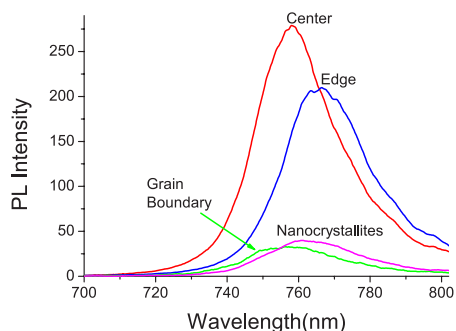

Figure 7: Tip-Enhanced Photoluminescence (TEPL) spectra taken from different locations of the WSe_2 flakes.

In the present example of several WSe_2 flakes merging at different angles, the dependence of the phonon and excitonic processes at the grain boundaries can be observed as a function of tilting angle at the nanoscale as well as their sensitivity to light.

Frequency modulated Kelvin probe measurements (FM-KPFM) are therefore conducted with the same silver coated tip as the TEPL measurements with the 633 nm laser illumination OFF and ON (Fig. 8). The contact potential difference (CPD) and the second derivative of capacitance ($\partial^2 C/\partial z^2$) with respect to the tip-sample distance (relative change of capacitance) signals are collected both with and without illumination. In the images, the GB show different CPD and $\partial^2 C/\partial z^2$ contrast depending on the angle of intersection. With no laser illumination some GB show higher CPD signal than basal plane while the GB between two flakes rotated by 180° (indicated as twin GB in Fig. 8) show lower CPD than basal plane. Under laser illumination the higher CPD-GB feature even higher CPD while twin GB show slightly higher CPD signal than basal plane. As for the $\partial^2 C/\partial z^2$ maps there is also clear contrast in GB signals depending on the tilting angles. The capacitance of twin GB is found to be more sensitive to light than other orientation as they appear clearly under illumination but are not visible in the laser OFF map. These two distinct types of contrast observed in CPD and $\partial^2 C/\partial z^2$ maps corresponding to "families" of tilting angles are consistent with the TEPL map also exhibiting GB with different contrast (Fig. 6c). This could be linked to different defects density and type as well as stoichiometry variation. In addition, it is important to note that the absence of GB between the flake in the bottom right of the map and the upper one corresponds to perfect lattice match and coincides with no contrast in CPD, $\partial^2 C/\partial z^2$, and PL maps.
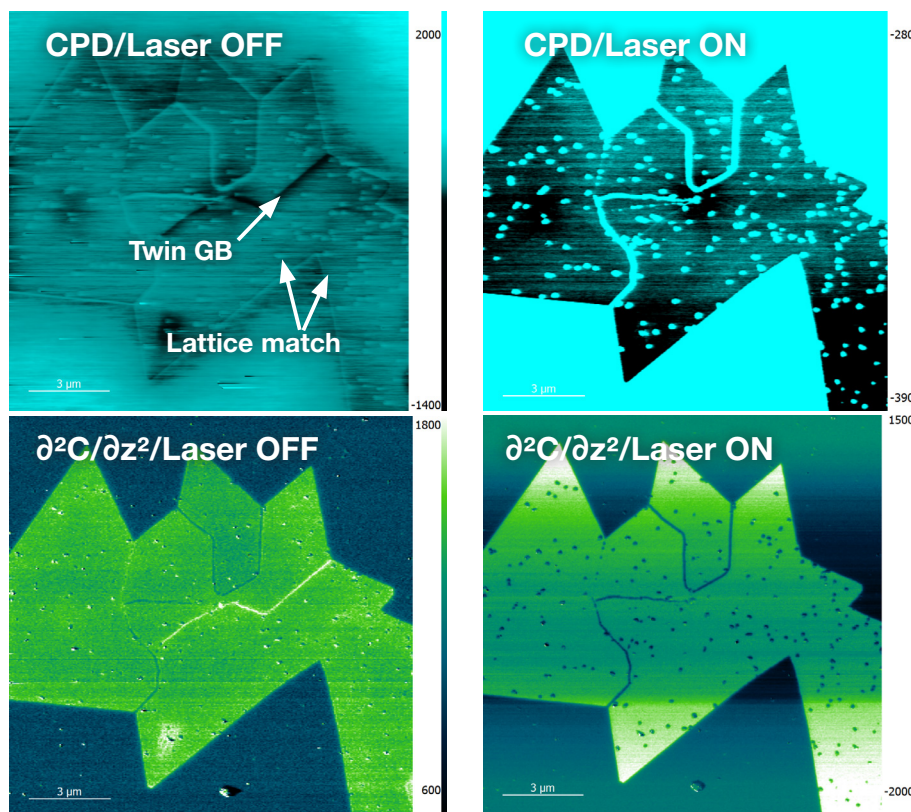

Figure 8: FM-KPFM measurements on the same WSe_2 flake showing contact potential difference (CPD) and the second derivative of capacitance ($\partial^2 C/\partial z^2$) under 633 nm laser illumination and without illumination.

Correlated TERS and SPM of WS₂ flakes on template stripped silver

WS₂ flakes are exfoliated on template stripped silver. Topography, phase shift, contact potential difference (CPD), and $\partial^2C/\partial z^2$ are measured with a NanoRaman™ system (HORIBA Scientific) in the dark for 5.5 x 5.5 µm images with 400 lines resolution (Fig. 9). Surface potential (CPD) image presented in Fig. 9 shows significant inhomogeneities of both the silver substrate and the WS₂ flake. TERS measurements are performed using a 638 nm *p*-polarized laser focused onto the vicinity of cantilever-based silver coated TERS tip.

Two Raman maps are acquired corresponding to "near-field + far-field" (NF+FF) and "far-field" (FF) using "S*pec-Top*™" mode with "dual spec" option. The acquisition time of each spectrum is 150 ms and pixel size is 44 nm. Fig. 10 shows the far-field (conventional µRaman) and near-field (TERS) images generated from the integration of 418 cm⁻¹ peak **(in blue)**, and the 347 cm⁻¹ peak **(in green)** corresponding to the A_{1g} and 2LA(M) bands, respectively. The µRaman image with a diffraction-limited optical resolution features the flake but with blurred contours and a homogeneous distribution of both Raman signal intensities.
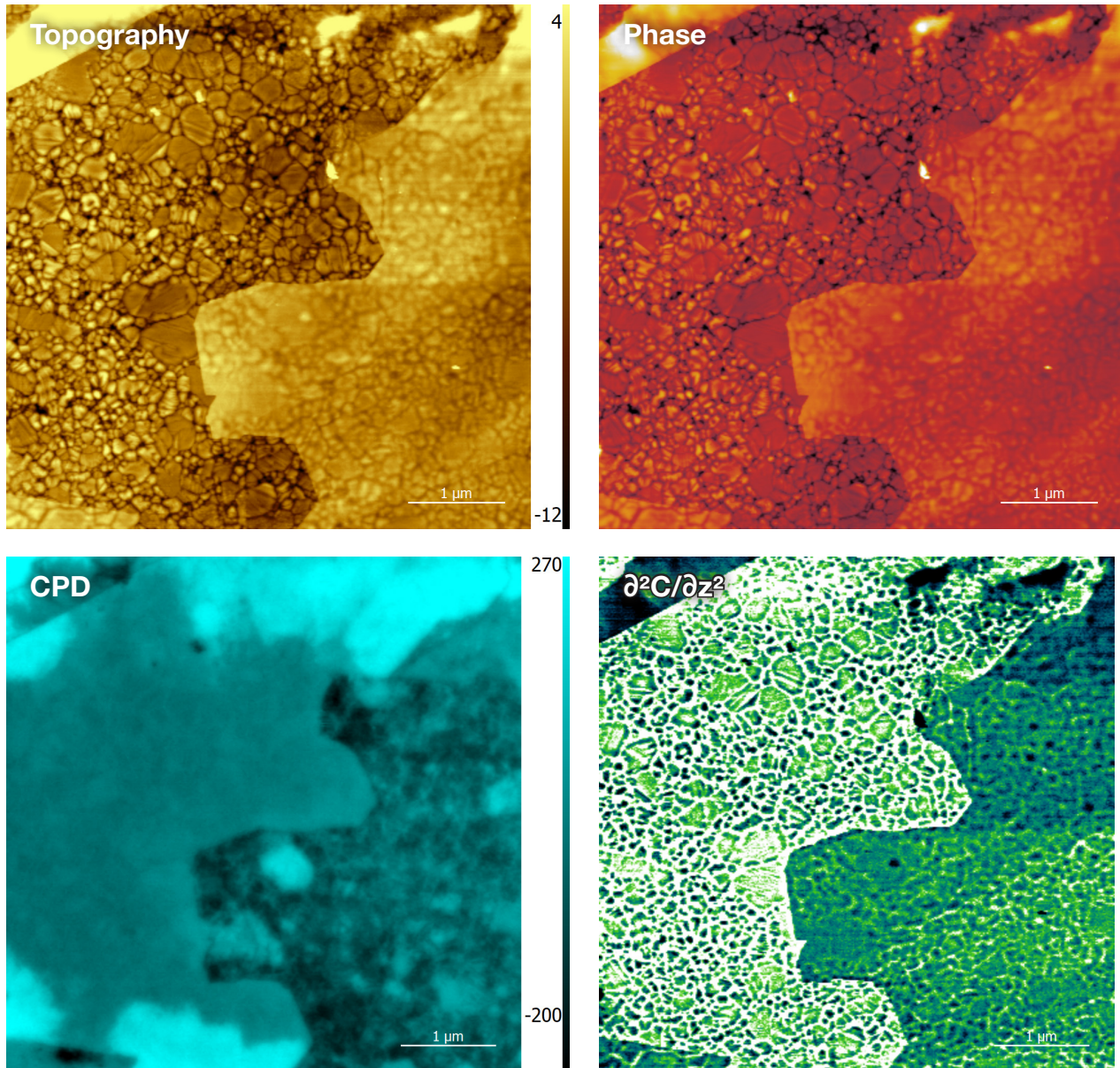

Figure 9: Topography, phase shift, CPD and $\partial^2C/\partial z^2$ measurements of WS₂ flake exfoliated on template stripped silver.

In contrast, the higher resolution TERS image reveals much more details (Fig. 10):

(i) Much sharper edges of the flake.
(ii) Inhomogeneities of the Raman signals, in particular of the A_{1g} peak (in blue) with the presence of dark nanodomains.

There are apparent correlations between the features in CPD and TERS images (Fig. 9 and Fig. 10). This is clearly illustrated with average spectra taken from 3 different areas with **positive** CPD (~ 50 meV **in red**), **negative** CPD (~ -100 meV **in green**), and **highly negative** CPD (~ -160 meV **in blue**) which exhibit **low and equal 2LA (M) and A_{1g} peaks, high 2LA (M)**, and **high A_{1g} peak**, respectively. In the areas with lower CPD, locally formed metallic phases suppress the TERS response. These correlations between surface potential (CPD) and TERS signatures indicates the presence of inhomogeneities within interfacial electronic properties, which are attributed to variations in the local doping of the WS_2 flakes [8].
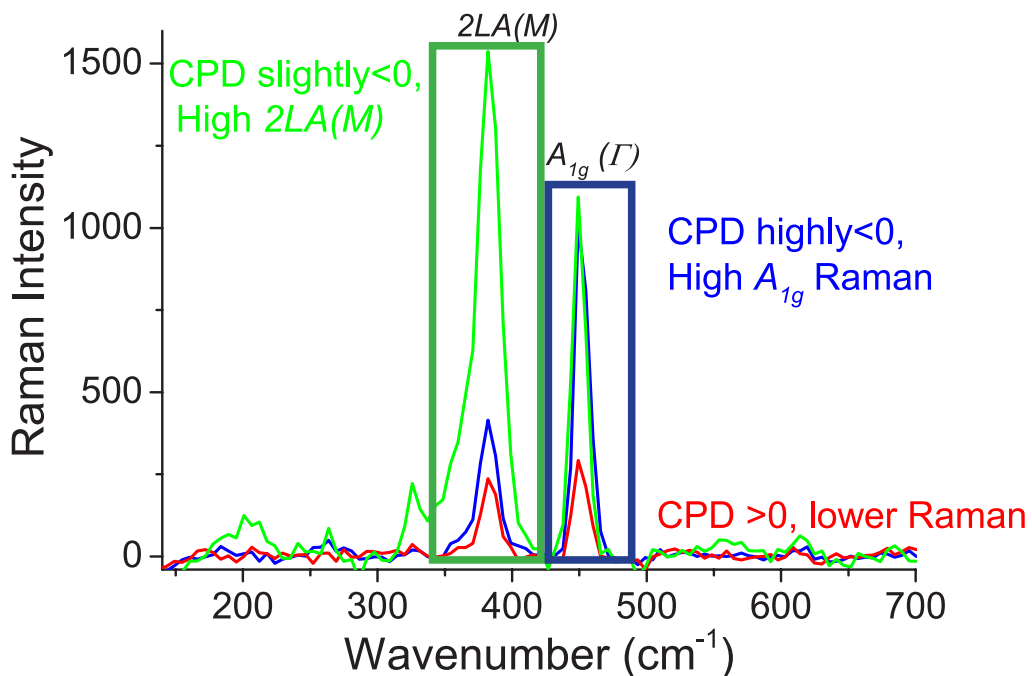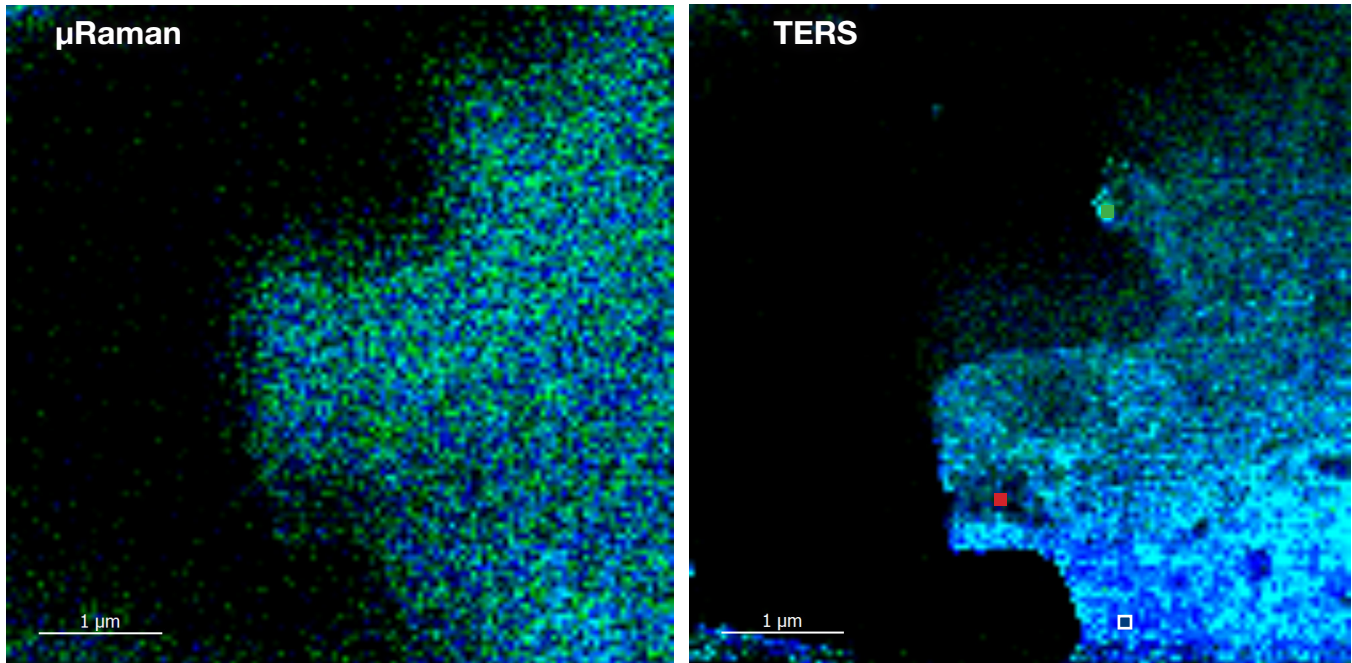

Figure 10: (Top) Conventional µRaman and TERS images of the same of WS_2 flake. (Bottom) Typical TER spectra taken from the square areas in the TERS image.

Correlated TERS and SPM of WSe_2 flakes on Au thin film

The understanding of charge transport and optimization of transistor mobility and current density in the fabrication of TMDCs based semiconductor devices requires study of semiconductor-insulator interfaces such as with SiO_2/Si. Equally important is the interface between the semiconducting TMDC and the contact metal, as it is the locus of charge carrier injection and collection. In this case the interface between WSe_2 and gold is probed using scanning probe microscopy (SPM) and TERS. The sample is prepared by mechanical exfoliation of WSe_2 on 120 nm thick gold.

A combination of topography, contact potential difference (CPD), TERS, and photocurrents maps is collected for nanoscale cross-correlations with a NanoRaman™ system (HORIBA Scientific) in a previously described configuration. In the AFM topography image (Fig. 11a), flakes with thicknesses in the range of 0.8-3 nm range can be seen, corresponding to 1-4 layers of WSe_2.
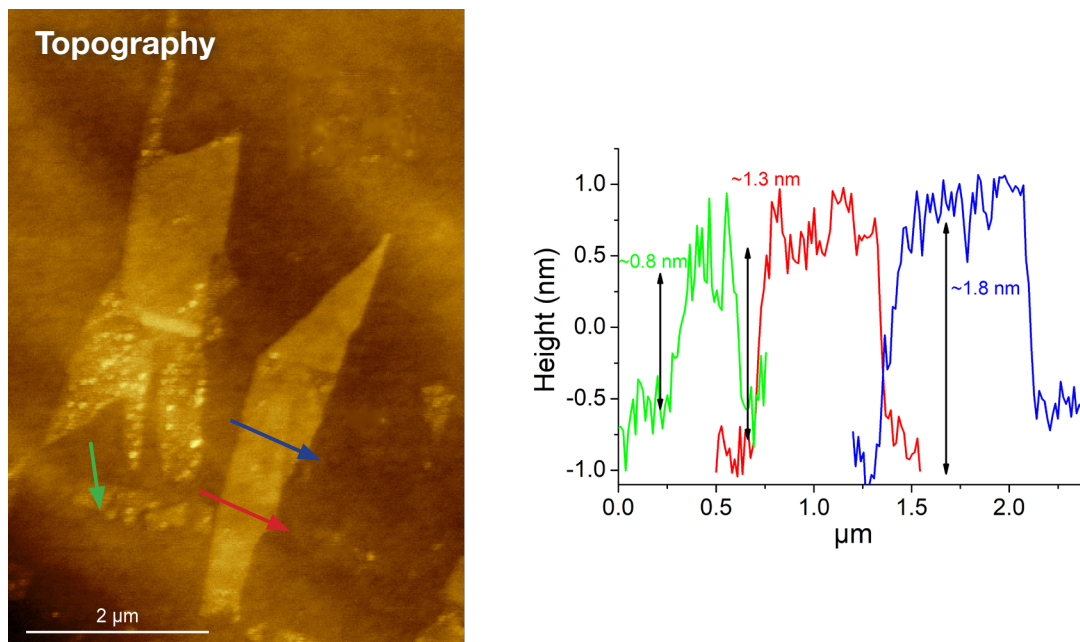

Figure 11a: AFM topography and height profiles of WSe_2 flakes on Au. The different colored profiles correspond to the arrows in the image.

Kelvin probe measurements in frequency modulation (FM-KPFM) mode are conducted in the same area. The contact potential difference (CPD) map (Fig. 11b) which gives the distribution of the surface potential across the sample tells us about the change in electronic properties of the material and about the presence of contamination layers. As shown in CPD image, variations in surface can be as high as 150 meV within a flake between adjacent domains.

The TERS map is also acquired on the same area of the sample in "*Spec-Top™*" mode. The **blue**-color map shown here is the intensity response of the large [217-262 cm^{-1}] band centered at 240 cm^{-1}. A striking observation occurs immediately when looking at the CPD and TERS map side by side (Fig. 11b, top). The TERS intensity map correlates extremely well with the CPD with high Raman intensity coinciding with higher surface potential and domains exhibiting low Raman intensity are also areas with lower surface potential. This is nicely illustrated by the graph plotting CPD and Raman intensity profiles on a line with variation of CPD as high as 150 meV and of Raman intensity of a factor 100 (Fig. 11b, bottom). Plotting two average TERS spectra from both high (**blue**) and low (**red**) CPD value areas evidences, in the high intensity area (**blue**) the presence of additional Raman peaks (LA(M) at 135 cm^{-1}, A(M) at 240 cm^{-1}, 2LA(M) at 260 cm^{-1} as well as complex peaks at around 375 cm^{-1} and 390 cm^{-1}) as a result of Raman resonant conditions met with the 638 nm excitation laser which overlaps with a broad shoulder on the high energy side of A exciton (1.74 eV; 712 nm). The lower CPD value areas exhibit non-resonant Raman with the single A_{1g}+E_{2g} peak. This correlation featuring nanoscale heterogeneities of the surface potential with matching Raman response is not feasible using conventional confocal Raman microscopy, for which the spatial resolution is limited by diffraction to approximately 400-500 nm at the 638 nm pump wavelength used in our experiments; clearly insufficient to resolve domains 10 nm-100 nm in lateral size.
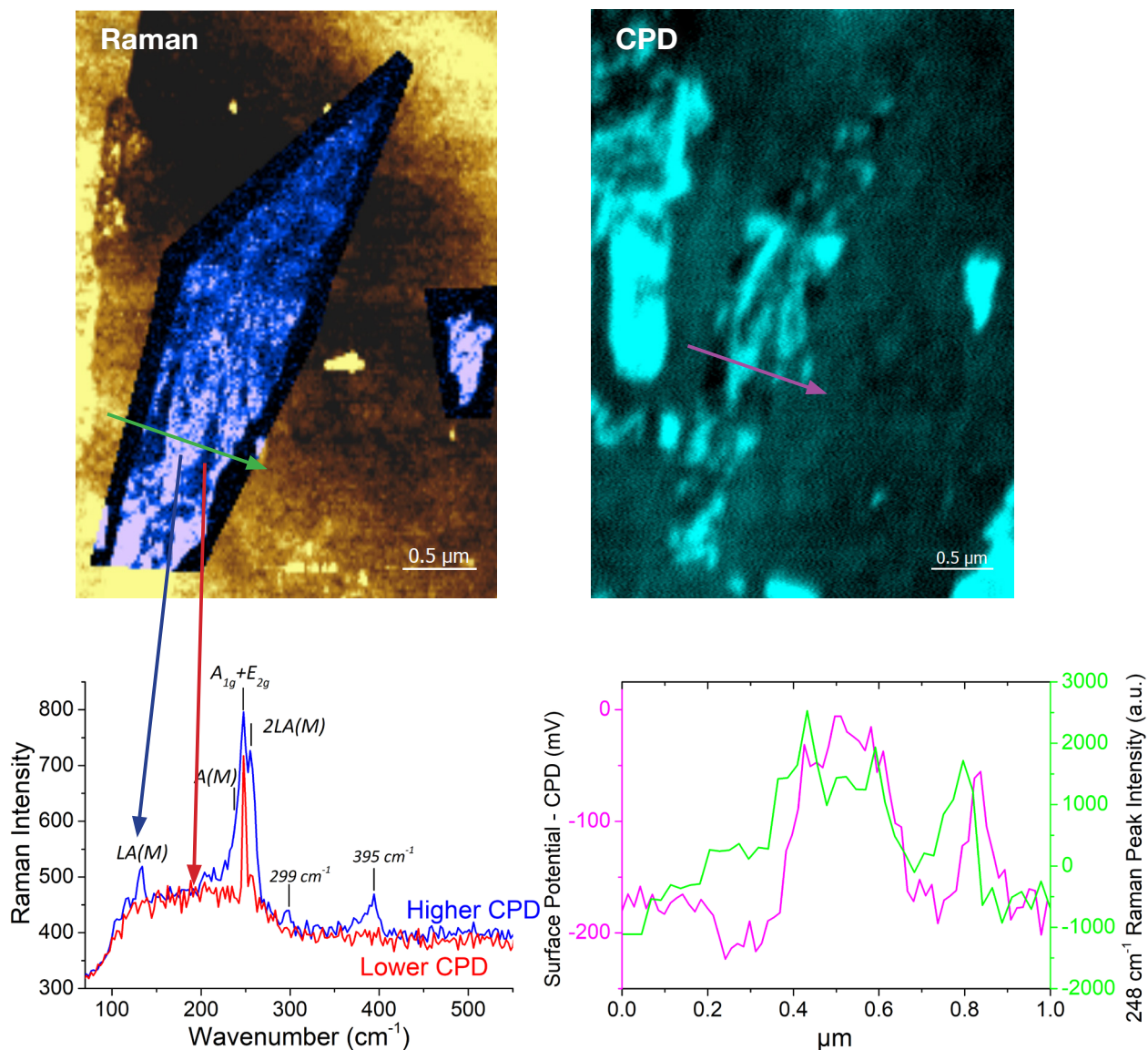
Figure 11b: Contact potential difference (CPD) and TERS images of the same WSe$_2$ flakes on Au. The different colored profiles correspond to the arrows in the images.

Complementary measurements of WSe$_2$ exfoliated on another metal, namely template stripped silver has shown nanoscale inhomogeneities with similar correlation between Raman and surface potential [9]. In addition, photocurrent measurements at the same nano-resolution confirm the semi-conducting nature of WSe$_2$ and that surface potential variation most likely results from intrinsic non-uniformity of the WSe$_2$ crystalline structure. Nanodomains with higher CPD have negative photocurrent and low CPD regions exhibit photocurrent of opposite sign, which can be interpreted as due to nanodomains having complementary doping type.

TEPL of WS$_2$/WS$_x$Se$_{1-x}$/WSe$_2$ heterostructure on SiO$_2$/Si

Building up nanodevices from 2D layered materials requires heterostructures. The electrical and optical properties of such heterojunctions will depend on the alignment of the energy bands at the interface. Using alloys of transition metal dichalcogenides allows for band gap engineering which is likely to lead to sharp and well controlled interfaces.
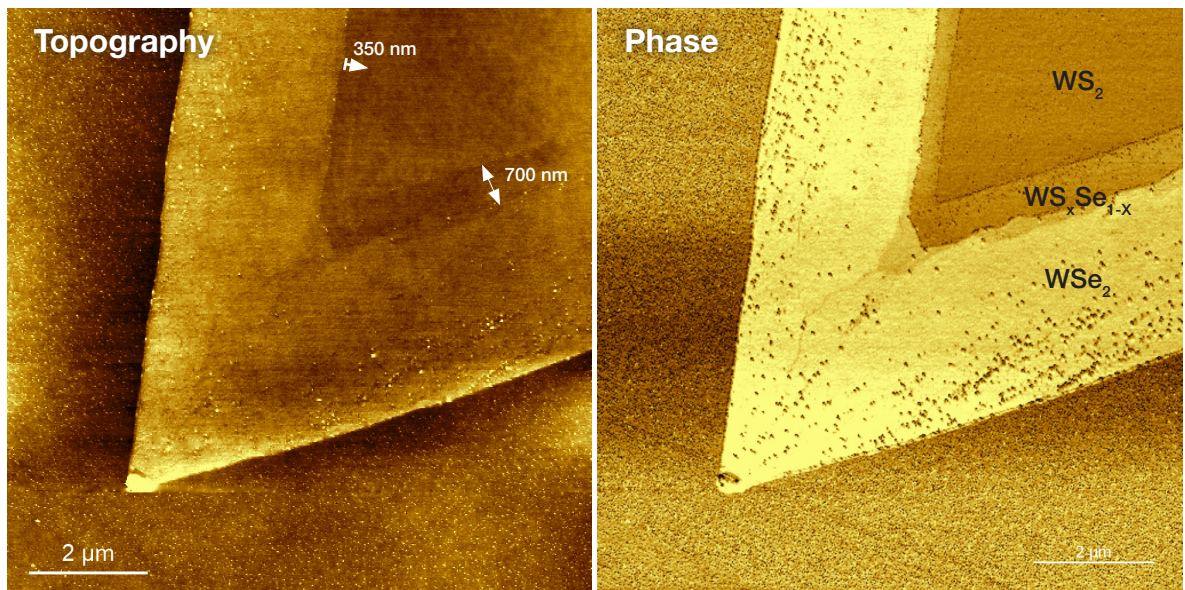
Figure 12: AFM topography and phase images of the 2D heterostructure.

TEPL has already been applied to the $MoSe_2$-WSe_2 heterojunction for the study of quantum plasmonic injection and aging effect [10, 11], here we present TEPL data obtained on a lateral single layer WS_2/WS_xSe_{1-x}/WSe_2 heterostructure grown on SiO_2/Si.

The 10×10 µm AFM topography and phase shift images (512 lines) show the apex of 60 µm triangular flake with a contrast allowing to distinguish the presence of both binary and ternary alloys (Fig. 12). The nicely defined interfaces seen on both images allow the width of the ternary WS_xSe_{1-x} layer to be measured: 700 nm on one side of the flake apex and 350 nm on the other side. The height profile (not shown)

across the three materials shows a rise of 0.6 nm from WS_2 to the ternary alloy, no measurable height change from the ternary alloy to the peripheral WSe_2, and a WSe_2 thickness of about 2.5 nm.

Tip-Enhanced Photoluminescence (TEPL) is performed using a NanoRaman™ system, 532 nm excitation laser and cantilever-based silver coated TERS tips. Two PL maps are acquired on the same run using "*Spec-Top™*" mode with "dual spec" option. The acquisition time of each spectrum is 50 ms and pixel size is 100 nm. A three color map (Fig. 13) including the TEPL response from **WS_2 (peak centered at 625 nm)**, **WS_xSe_{1-x} (peak centered at 665 nm)**, **WSe_2**
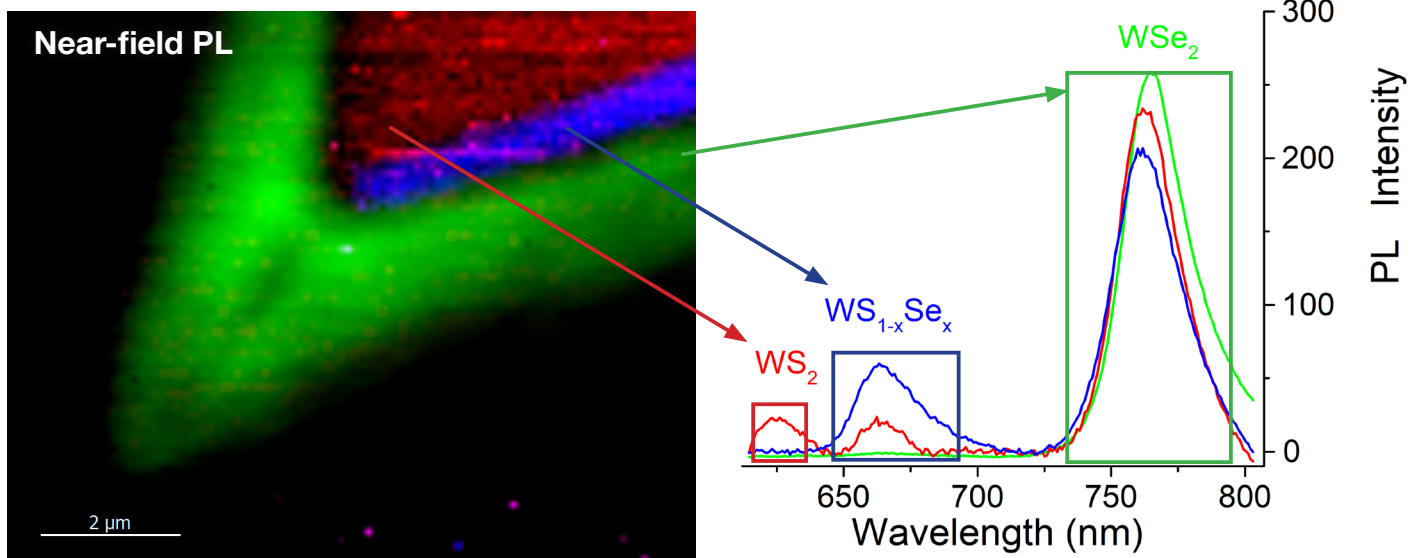

Figure 13: (left) TEPL (aka near-field PL) of the WS_2/WS_xSe_{1-x}/WSe_2 heterostructure on SiO_2/Si, (right) TEPL spectra from different regions of the heterojunction.

(peak centered at 765 nm) confirms the presence of the three single layer compounds as well as a difference in the WS_xSe_{1-x} PL signal quenched on the left side of the apex (appearing narrower on the height and phase shift images). The graph showing average spectra from the three regions indicates the integration PL response intervals (Fig. 13, right).

Two true TEPL maps (far-field subtracted) are generated for the **WS_xSe_{1-x} PL** and the **WSe_2 PL** responses and are overlaid with an AFM topography map (Fig. 14). The **WSe_2 TEPL** map shows some inhomogeneities due to excitonic heterogeneities at the nanoscale as illustrated by the signal profile (insert in Fig. 14). These nanoscale variations could not be seen in the topography and phase shift images. The
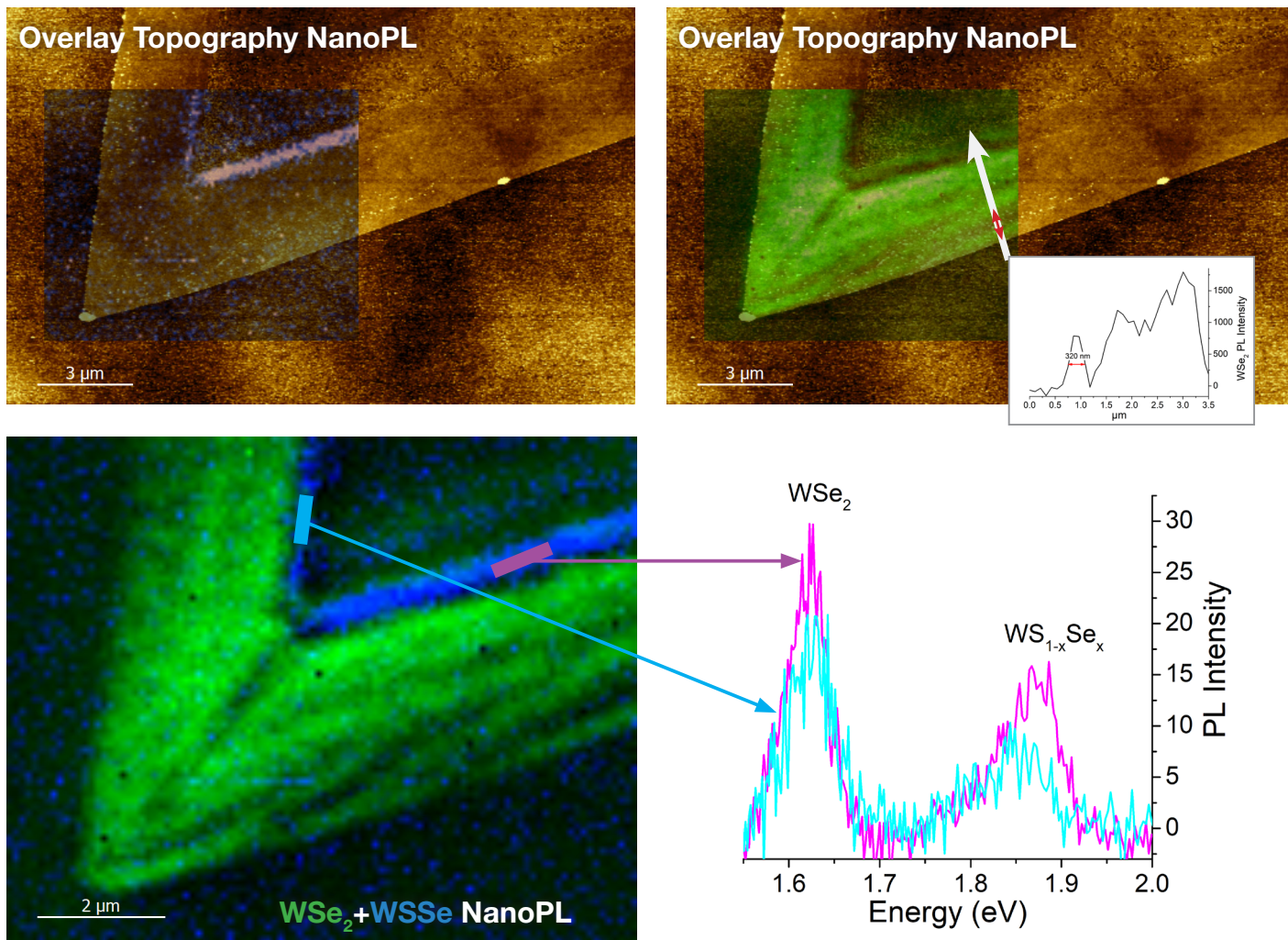
WS_xSe_{1-x} TEPL map shows an intense ~600 nm wide stripe for the right-side alloy and a much less intense and narrower stripe on the left side of the flake apex.

This correlates well with the first observations from the AFM images. The graph comparing average spectra extracted from both regions gives some further insight with PL response for the left side being shifted to lower energy (1.84 eV versus 1.87 eV for the right side). The observed PL peak shift is associated with the alloying across the interfaces, the observed peak shift can be directly linked to the change in alloy composition.

Figure 14: (Top) Overlay of AFM topography with (left) WS_xSe_{1-x} TEPL and (right) WSe_2 TEPL images. (Bottom left) Overlay of WSSe and WSe_2 PL. (Bottom right) Typical spectra from the WSSe regions.

Conclusions

In this application note, we have presented new nano-imaging capabilities with correlated TERS, TEPL and SPM measurements of different 2D materials and heterojunction. We have demonstrated that TEPL, not limited by diffraction, provides a drastic improvement of the optical resolution compared to conventional far-field photoluminescence (microPL) and is also more accurate than AFM topographic imaging to confirm the presence of transferred MoS_2 monolayer flakes. Single crystal WS_2 and WSe_2 flakes directly grown on SiO_2/Si have been also analyzed with TEPL: NanoPL response maps nicely overlay on topography images (monolayer, bilayer, nanocrystallites). Moreover, we have shown the sensitivity of electronic properties (contact potential and capacitance related to Fermi level and charge accumulation) upon light illumination. Beside these semiconductor/dielectric (SiO_2) interfaces, results from probing TMCD/metal interfaces, namely WS_2 on silver and WSe_2 on gold have been also shown. TERS and Kelvin probe measurements revealed nanoscale inhomogeneities both observed in CPD and Raman maps. Finally, NanoPL together with AFM topography data on a lateral single layer WS_2/$WSxSe_{1-x}$/WSe_2 heterostructure grown on SiO_2/Si have been presented and revealed nanoscale PL response variations beyond the smooth nano-resolution topography.

References

[1] Nature Communications 9, 2891 (2018).
[2] ACS Appl. Nano Mater. 1 (2), 572 (2018).
[3] Nanoscale 10, 14055 (2018).
[4] Nanoscale 10, 2755 (2018).
[5] Nano Lett.17 (10), 6027 (2017).
[6] Phys. Rev. B 97, 085305 (2018).
[7] 2D Mater. 4, 021024 (2017).
[8] Sci. Adv. 5:eaau8763 (2019).
[9] 2D Mater. 5 035003 (2018).
[10] Phys. Rev. B 98, 041402(R) (2018).
[11] Opt. Mater. Express 9, 1620 (2019).

Acknowledgments
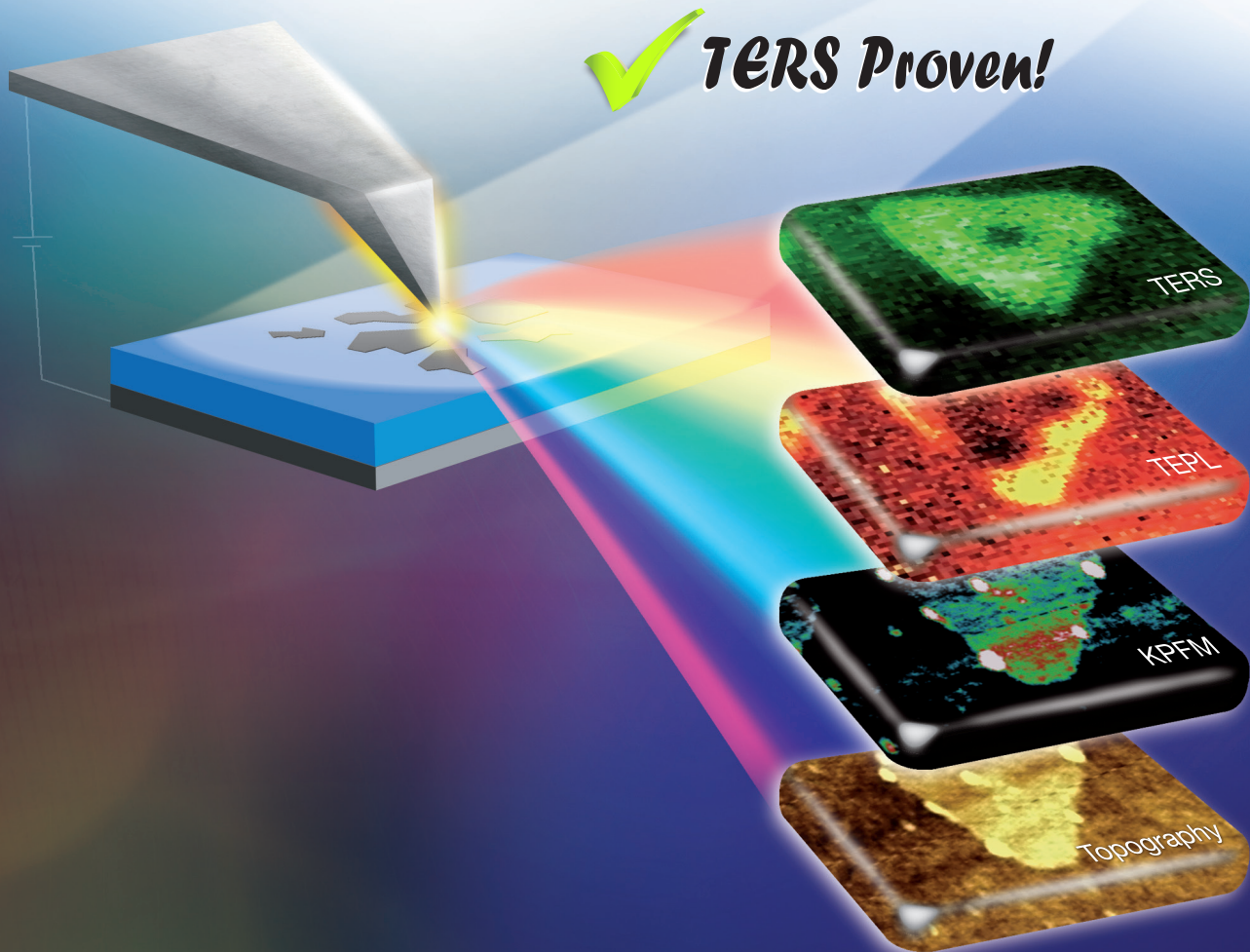
NanoRaman™: When Atomic Force Microscopy Integrates Optical Spectroscopy

- ☑ Multi technique analysis platform from macro to nanoscale
- ☑ True Confocal Raman spectroscopy
- ☑ Robust, stable, ultimate resolution in AFM
- ☑ Multi-user friendly, short time to results

www.horiba.com/nanoraman | info-sci.fr@horiba.com

Explore the future   Automotive Test Systems I Process & Environmental I Medical I Semiconductor I Scientific   **HORIBA**

HORIBA
Scientific

HORIBA JOBIN YVON

Find out more at www.horiba.com/nanoraman

Worldwide Training and Technical Support

Jobin Yvon, established in 1819, and now part of the HORIBA Scientific is one of the world's largest manufacturers of analytical and spectroscopic systems and components.

The HORIBA Scientific teams are committed to serving our customers with high performance products and superior technical support.

Our staff of experienced application and service engineers, located around the world, provides full support for your instrument and its future upgrades.

Well equipped application laboratories allow for sample analysis and hands-on training for new and experienced users.

HORIBA Worldwide

www.ramanacademy.com

Free learning tools for new and experienced Raman users.
Available to anyone who is interested in learning more about Raman.

λ = 325-1064nm P ≤ 500mW
VISIBLE AND/OR INVISIBLE LASER RADIATION
AVOID EXPOSURE TO BEAM
CLASS 3B LASER PRODUCT

CE

Explore the future   Automotive Test Systems I Process & Environmental I Medical I Semiconductor I Scientific   **HORIBA**